

Highly Sensitive and Fast-Response Hybrid Phototransistors Enabled by Dynamic Photogating in Anthradithiophene-Metal Oxide Heterojunctions

Ahasan Ullah, Roshell Lamug, Xueqiao Zhang, Oksana Ostroverkhova, and Li-Jing Cheng*

This study presents a high-performance organic–inorganic hybrid phototransistor featuring a heterojunction formed by photoactive anthradithiophene (ADT) derivatives and a bottom-gate indium gallium zinc oxide (IGZO) thin-film transistor (TFT). Two ADT derivatives with silicon- or germanium-containing side chains are explored for device development. The band alignment at the heterojunction facilitates efficient electron transfer and accumulation of photogenerated holes in ADT, driving a photogating effect to modulate IGZO conductivity. Unlike conventional photogating, mediated by carrier trapping with inherently slow response speeds, this device uses trap-suppressed ADT, achieved through blending with nonconductive polymers, to enable high-speed photogating. An optimized negative gate voltage creates a synergistic effect, driving the IGZO TFT into a partially depleted subthreshold state and significantly enhancing detectivity and sensing current. Photoluminescence and wavelength-dependent photoresponse confirm charge transfer between ADT and IGZO, identifying the photoinduced threshold voltage shift as the key mechanism for improved performance. Simulations further elucidate the photodetection process under varying conditions. The phototransistor achieves a linear dynamic range over 100 dB, responsivity of up to 2.80 A W^{-1} , detectivity exceeding 10^{13} Jones, and rapid response with $<4 \text{ ms}$ rise and $<10 \text{ ms}$ fall times. These characteristics make it highly suitable for machine vision and low-power photosensor applications.

communication.^[1,2] Among the various materials explored, organic semiconductors stand out as promising candidates for photosensors due to their tunable optical properties through molecular modification, cost-effective production via solution processing, scalability for manufacturing, and flexibility in integrating into diverse applications.^[3–7] In particular, small molecule solution-processable organic semiconductors have gained significant attention for their potential in organic thin-film transistors (TFTs) and photosensors.^[8] Their solubility in various solvents and ease of processing make them appealing for flexible and large-area (opto)electronics. Strategies for improving the chemical stability and environmental resistance of organic semiconductors have shown progress.^[9,10] Nevertheless, typical limitations of organic semiconductors—such as low carrier mobility and charge trapping—continue to hinder device response and performance compared to inorganic materials.^[11] To overcome these drawbacks, integrating organic semiconductors with inorganic materials like indium gallium zinc oxide (IGZO) presents a promising approach.^[12] IGZO, a metal

oxide known for its high electron mobility and visible-range transparency, has been instrumental in advancing TFT technology.^[12] By integrating the photoactive sensitivity of an organic semiconductor with the high carrier mobility of IGZO, which lacks intrinsic visible-range photosensitivity, the hybrid structure capitalizes on the strengths of both materials to achieve enhanced photodetection performance unattainable by either material alone.

As the organic photosensitive layer, we chose 2,8-difluoro-5,11-bis(triethylsilylethynyl) anthradithiophene (diF-TES-ADT, referred to as TES-ADT) and its germanium-containing counterpart, 2,8-difluoro-5,11-bis(trialkylgermyl)anthradithiophene (diF-TEG-ADT, referred to as TEG-ADT), shown in Fig. 1(b). These materials are benchmark solution-processable, stable p-type organic semiconductors with studies reporting charge carrier mobilities exceeding $1 \text{ cm}^2 \text{ V}^{-1} \text{ s}^{-1}$. In optimized TFTs, they have demonstrated mobilities of up to $20 \text{ cm}^2 \text{ V}^{-1} \text{ s}^{-1}$, attributed to improved film microstructure and reduced contact resistance.^[13–15]

1. Introduction

The advancement of photosensing technology has played a crucial role in driving applications, from image sensors to more sophisticated systems for spectral analysis and optical

A. Ullah, X. Zhang, L.-J. Cheng
School of Electrical Engineering and Computer Science
Oregon State University
Corvallis, OR 97331, USA
E-mail: chengli@oregonstate.edu

R. Lamug, O. Ostroverkhova
Department of Physics
Oregon State University
Corvallis, OR 97331, USA

 The ORCID identification number(s) for the author(s) of this article can be found under <https://doi.org/10.1002/adom.202500081>

DOI: 10.1002/adom.202500081

Both TES-ADT and TEG-ADT crystallize into 2D “brickwork” structures, which support efficient charge transport. TEG-ADT exhibits 0.13 Å lower interplanar spacing, 1.8 Å smaller long-axis shift between adjacent molecules, and 11% higher areal overlap compared to TES-ADT, resulting in higher charge carrier mobility for TEG-ADT.^[15] Blends of R-ADT (ADT derivatives with various side groups R) with nonconductive “binder” polymers have demonstrated superior TFT charge carrier mobilities compared to pristine R-ADT TFTs. This improvement is attributed to enhanced film morphology in the blends, effectively suppressing the formation of traps at grain boundaries.^[16,17] Additionally, R-ADT films and crystals have been extensively studied under light excitation, demonstrating efficient singlet fission,^[18] high photoconductivity,^[19,20] and strong performance in phototransistors.^[21,22] Solution-deposited blends of small-molecule organic semiconductors (such as TIPS-pentacene or R-ADT) with polymers exhibit morphologies dependent upon the solvent boiling point, polymer crystallinity, molecular weight, and concentration, as well as the deposition conditions,^[23,24] with crystalline and high-molecular-weight binder polymers promoting vertical segregation of the polymer and small-molecule layers.^[17,25,26] Instead, spin-cast blends of a low concentration of low-molecular-weight (<100 kDa) amorphous binder polymer, such as PMMA, with TES-ADT form an interconnected network of aggregates that maintain photocurrents comparable to pristine TES-ADT films.^[27] This approach also facilitates the production of a uniform film thickness, enabling polariton formation within resonant microcavities in these blends.^[28]

The ADT-capped IGZO TFT creates a heterojunction with favorable band alignment, facilitating charge separation. Photogenerated electrons are transferred to IGZO, while holes accumulate in ADT, creating an electric field that modulates IGZO’s conductivity and enhances phototransistor performance. This approach, also referred to as the photogating effect in some similar systems, provides a more sensitive photodetection signal compared to conventional photosensors, which rely solely on measuring the current from photogenerated carriers.^[29,30] Previous studies have highlighted the critical role of heterojunction interfaces in device performance, affecting charge separation, transport dynamics, and recombination processes.^[31] Photodetectors utilizing the photogating effect have been explored using various light absorber capping layers, such as polymer semiconductors (PBDTT-DPP: PC61BM), perovskite (MaPbI₃), and quantum dots.^[32–34] These devices, which typically rely on the trapping of photogenerated carriers to modulate channel conductivity, often exhibit slower response speeds due to prolonged recovery times associated with carrier de-trapping.^[35]

Hybrid phototransistors based on TES-ADT/IGZO and TEG-ADT/IGZO heterojunctions overcome these limitations by utilizing trap-suppressed ADT in polymer blends, optimized IGZO processing and a polymer-passivated interface to minimize defects and slow trapping. The photogating effect was achieved directly through the accumulation of photoexcited holes, enabling faster modulation of device conductivity compared to trap-mediated mechanisms. Leveraging the synergy with an optimally tuned gate voltage (V_g), the devices exhibit significant improvements in responsivity, detectivity, and linear dynamic range (LDR) compared to traditional counterparts. While TES-ADT and TEG-ADT share structural similarities, subtle differences in their

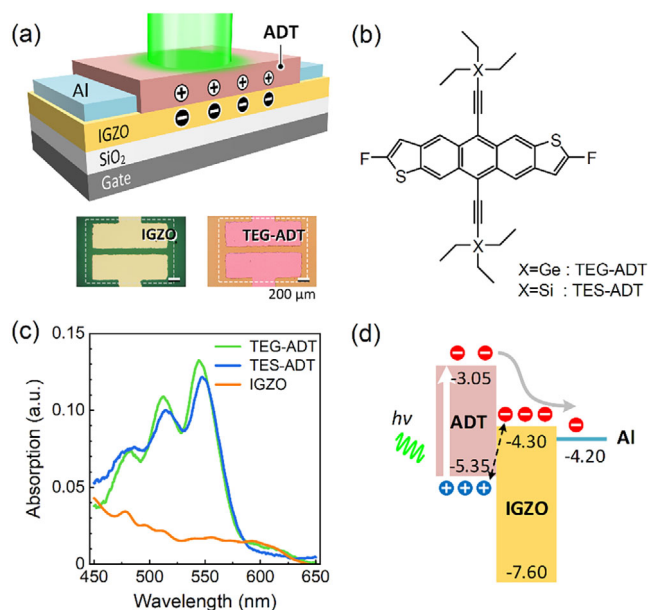


Figure 1. a) Schematic of the ADT/IGZO heterojunction phototransistor with enhanced detection capabilities enabled by a photogating effect. Inset displays the optical images of the IGZO TFT before and after TEG-ADT spin coating. The dashed line outlines the IGZO region. b) Molecular structure of TES-ADT and TEG-ADT. c) Absorption spectra of IGZO, TES-ADT, and TEG-ADT films. d) Energy diagram of the ADT/IGZO junction illustrating the transfer of photogenerated electrons to IGZO and accumulation of holes in ADT, which electrostatically induces additional electrons in IGZO, leading to the photogating effect.

molecular packing and film crystallinity (Figure S1, Supporting Information), previously shown to affect carrier mobilities,^[15,36] result in distinct responses in heterojunction devices. Experimental studies and simulations further elucidate the mechanisms behind the enhanced performance, highlighting the potential of hybrid organic-inorganic phototransistors to advance photosensor technology beyond conventional designs.

2. Results and Discussion

2.1. Device Structure and Photodetection Characteristics

Figure 1a illustrates the ADT/IGZO heterojunction TFT with a bottom-gate, top-contact configuration. The inset shows the microscope images of the IGZO TFT before (left) and after (right) ADT coating. The gap between the source and drain electrodes defines a channel length of 100 μm, with a channel width of 1000 μm set by the electrode width. Figure 1c shows that both TES-ADT and TEG-ADT exhibit similar absorption spectra, featuring three distinct excitonic peaks at 545, 512, and 482 nm. These peaks suggest aggregate or crystallite formation, consistent with the crystalline order observed in the X-ray diffraction data (Figure S1, Supporting Information).^[17,28,37] In contrast, IGZO remains largely transparent over the visible range, showing only a slight absorption increase at shorter wavelengths. Both TES-ADT and TEG-ADT share similar molecular orbital energies, with a lowest unoccupied molecular orbital (LUMO) at −3.05 eV and a highest occupied molecular orbital (HOMO) at

−5.35 eV, as determined in our previous work.^[19] As depicted in Figure 1d, these ADT derivatives form a type II heterojunction with IGZO, which has a conduction band minimum of −4.30 eV and a valence band maximum of −7.60 eV.^[32] The band alignment positions ADT as the donor and IGZO as the acceptor, promoting charge separation. The ADT layer absorbs light and generates excitons, which can either recombine or dissociate. The heterojunction's band alignment ensures that electrons are transferred to the IGZO channel, while holes remain confined in the ADT layer. The accumulated holes in ADT create an electric field that shifts the TFT threshold voltage, significantly enhancing the device's photosensitivity.

Figure S2 (Supporting Information) shows that the bare IGZO TFT, without the organic photosensitive ADT layer, exhibited a field-effect mobility of $4.32 \text{ cm}^2 \text{ V}^{-1} \text{ s}^{-1}$ and an $I_{\text{on}}/I_{\text{off}}$ ratio greater than 10^7 . Notably, the ADT/IGZO phototransistors exhibited a higher field-effect mobility of $7.63 \pm 0.25 \text{ cm}^2 \text{ V}^{-1} \text{ s}^{-1}$ and a negative shift in threshold voltage of $\approx -1 \text{ V}$ compared to the bare IGZO TFT under dark conditions. The enhanced mobility and negative threshold voltage shift are likely due to the organic layer acting as a passivation layer on the IGZO surface.^[38] Figure 2a,b display the transfer characteristics of TEG-ADT/IGZO and TES-ADT/IGZO heterojunction phototransistors, respectively, measured in the dark and under 450, 560, and 600 nm light at a fixed power density of $40 \mu\text{W cm}^{-2}$. A consistent drain voltage (V_d) of 5 V was applied across all devices throughout the study. The phototransistors demonstrated a substantial photocurrent increase in the subthreshold regime, with the maximum current change observed at a V_g of -1 V . Under 450 nm light, the current rose from 4 pA to 28 nA, and under 560 nm, it reached 95 nA, while minimal response was observed at 600 nm. Likewise, TES-ADT/IGZO devices exhibited an increase from 4 pA to 32 nA at 450 nm and to 78 nA at 560 nm. Conversely, the bare IGZO TFT was insensitive to all these visible wavelengths under the same illumination conditions, as shown in Figure 2c. The significant current increase at negative V_g in illuminated ADT/IGZO heterojunction phototransistors results from a negative threshold voltage shift and increased subthreshold swing with photoexcitation, characteristic of the photogating effect.

The responsivity (R) for all devices at $V_g = -1 \text{ V}$ was calculated using the Equation (1)

$$R = \frac{I_{\text{ph}} - I_{\text{dark}}}{P_{\text{in}}} \quad (1)$$

where I_{ph} and I_{dark} are the drain currents under illumination and in the dark, respectively, and P_{in} is the incident optical power on the active device area. All responsivity measurements were conducted under $40 \mu\text{W cm}^{-2}$ illumination with a device active area of $100 \mu\text{m} \times 1000 \mu\text{m}$. The wavelength-dependent responsivities in Figure 2d,e show that TEG-ADT/IGZO and TES-ADT/IGZO devices responded to wavelengths below 575 nm, with negligible sensitivity for wavelengths above 600 nm, consistent with the absorption spectra of TEG-ADT and TES-ADT. In contrast, the bare IGZO TFT showed no photosensitivity across the visible spectrum, confirming that the photoresponse originated from the ADT organic layer. The TEG-ADT/IGZO device achieves a maximum responsivity of 2.80 A W^{-1} at 515 nm, while the TES-ADT/IGZO device reaches a peak of 2.27 A W^{-1} at 545 nm.

IGZO exhibits increased optical absorption for wavelengths below 450 nm, driven primarily by shallow trap states rather than its bandgap of 3.3 eV (376 nm), which effectively absorbs only wavelengths shorter than 376 nm. These trap states play a key role in enhancing photon absorption and free charge generation in the sub-bandgap region.^[39] Figure S3 (Supporting Information) presents the responsivity of the two heterojunction devices and bare IGZO devices in this wavelength range. Notably, the bare IGZO TFT displayed higher responsivity than the two heterojunction devices at near-UV wavelengths because IGZO primarily governs the photoresponse in this range. In the heterojunction devices, the ADT layer over the IGZO channel absorbed additional UV light, reducing IGZO's photoabsorption. As a result, even though IGZO had enhanced optical absorption and free carrier generation at near-UV wavelengths, the heterojunction devices exhibited lower responsivity.

Charge transfer from the ADT layer to IGZO was confirmed by photoluminescence (PL) analysis under identical low-power optical excitation to avoid photobleaching. Figure 2f shows significant PL quenching for both ADT derivatives when deposited on IGZO, compared to those on glass. This quenching was attributed to an efficient exciton relaxation pathway through charge transfer to IGZO, which reduced radiative recombination. To ensure a fair comparison with uniform ADT thickness on both IGZO and glass, the ADT layers were spin-coated on glass substrates partially deposited with IGZO.

Figure 2g,h presents the transfer characteristics of TEG-ADT/IGZO and TES-ADT/IGZO phototransistors under varying illumination power densities. Increased optical irradiance induced a negative shift in threshold voltage and a significant rise in subthreshold swing (or reduction in subthreshold slope) for both devices. These effects, driven by the type II heterojunction between ADT and IGZO (Figure 1d), greatly enhance photosensitivity, setting these phototransistors apart from conventional counterparts that primarily detect light through changes in off current. The detailed working mechanism will be discussed in the next section.

The substantial energy barrier between the aluminum source-drain contacts with a work function of -4.2 eV and the HOMO of ADT (-5.35 eV), inhibits efficient hole conduction through ADT.^[40] As a result, minimal photoconductivity was expected in the ADT layer, with the current primarily conducted through the IGZO channel. To confirm this, we characterized bare ADT phototransistors without IGZO under identical device dimensions and operating conditions as the heterojunction devices (Figure S4, Supporting Information). As shown in Figure 2i, under $350 \mu\text{W cm}^{-2}$ optical excitation, both bare TEG-ADT and TES-ADT phototransistors exhibited very low on-currents ($\approx 0.1 \text{ nA}$ at $V_g = -10 \text{ V}$). This confirms that photoresponsivity in the heterojunction phototransistors originated entirely from the IGZO channel conducting carriers generated or induced by the photoactive ADT layer.

2.2. Device Operation Mechanism

Light excitation generates excitons in the 50 nm-thick ADT layer, which either dissociate into carriers or reach the ADT/IGZO interface as excitons, where a strong internal electric field from

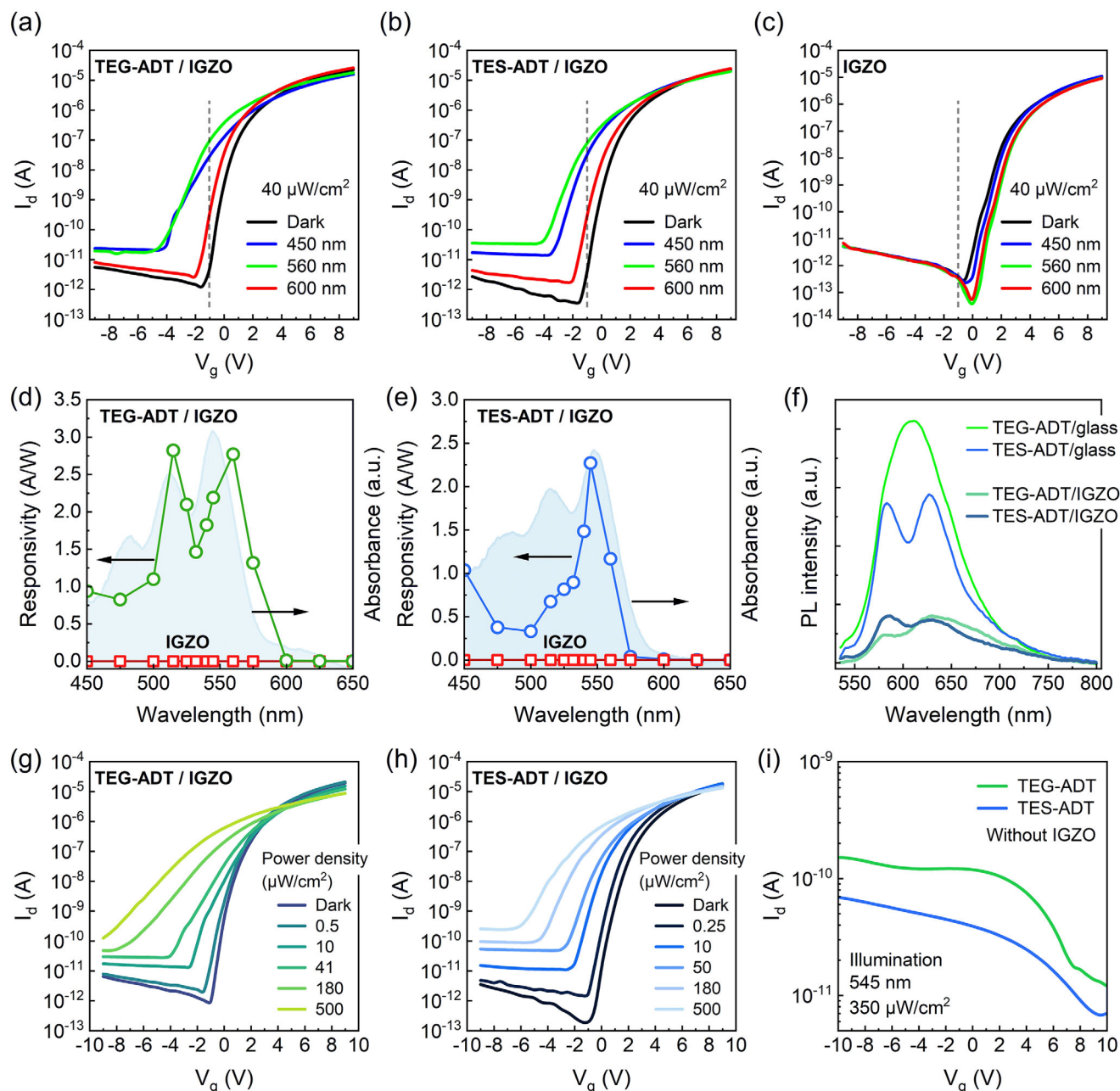


Figure 2. Transfer characteristics of a) TEG-ADT/IGZO and b) TES-ADT/IGZO heterojunction phototransistors, and c) pristine IGZO TFT, measured at $V_d = 5$ V in the dark and under 450, 560, and 600 nm illuminations at $40 \mu\text{W cm}^{-2}$. Dashed lines in each plot represent $V_g = -1$ V. Wavelength-dependent responsivity of the d) TEG-ADT/IGZO and e) TES-ADT/IGZO heterojunction devices along with the pristine IGZO TFT evaluated at $V_g = -1$ V, with corresponding TEG-ADT and TES-ADT absorbance spectra overlaid for comparison. f) Photoluminescence (PL) spectra of TEG-ADT and TES-ADT on glass and IGZO. Transfer characteristics of g) TEG-ADT/IGZO and h) TES-ADT/IGZO heterojunction phototransistors measured at $V_d = 5$ V in the dark and under 545 nm illumination at various power densities, and i) TEG-ADT and TES-ADT TFTs measured at $V_d = 5$ V under 545 nm illumination at $350 \mu\text{W cm}^{-2}$.

the staggered band alignment promotes dissociation. This band alignment, driven by the electron affinity difference between ADT (3.05 eV) and IGZO (4.3 eV), facilitates exciton dissociation, promotes electron transfer from ADT to the IGZO conduction band, and confines holes in ADT due to the energy barrier created by the energy band offset, as illustrated in **Figure 3a**. Under illumination, photogenerated holes accumulate in ADT,

electrostatically attracting electrons in IGZO to the heterojunction interface and increasing their concentration, a phenomenon known as the photogating effect. Additionally, electron transfer from ADT further increases the electron concentration in IGZO. The photogating effect plays a more dominant role in modulating IGZO conductance compared to electron transfer-induced changes in IGZO electron concentration. However, it can

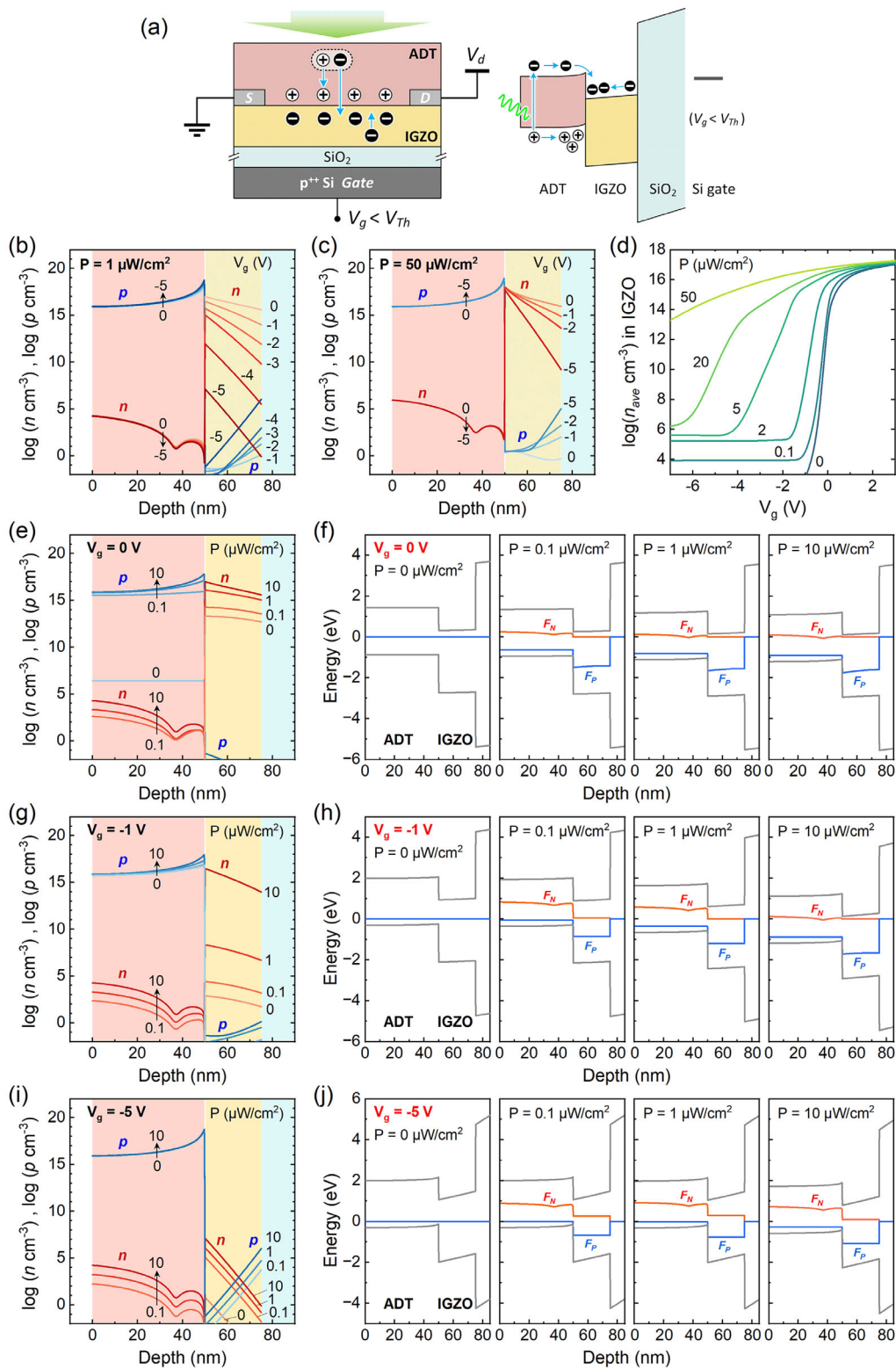


Figure 3. a) Photodetection mechanism of an ADT/IGZO heterojunction phototransistor. Electron (n) and hole (p) concentration profiles across the ADT layer (0–50 nm, red) and IGZO layer (50–75 nm, yellow) at varying V_g under 560 nm illumination of b) 1 and c) $50 \mu\text{W cm}^{-2}$. d) Average electron concentration in IGZO versus V_g under various illumination power densities at 560 nm. Electron (n), hole (p) concentration profiles, and energy band diagrams at V_g of e,f) 0 V, g,h) -1 V , and i,j) -5 V under various illumination power densities. The energy in the band diagram represents the electron potential energy relative to the gate electrode. Red lines and blue lines in the band diagram represent the quasi-Fermi levels for electron (F_N) and hole (F_P), respectively.

compete against the field effect of the applied V_g , impacting the efficiency of IGZO conduction modulation in response to photoexcitation. The TCAD simulation results in Figure 3, showing calculated electron and hole concentration profiles along with band diagrams, provide insights into the phenomena. Details of the simulation methodology are provided in the Supporting Information, with the device structure setup shown in Figure S5 (Supporting Information) and the simulation parameters summarized in Tables S1 and S2 (Supporting Information). The simulation results align with experimental trends and shed light on the device's operation, specifically elucidating how photogating and the applied V_g synergistically influence carrier concentration in the channel, directly affecting the photodetection responsivity. All simulations were conducted with $V_d = 0$ V to isolate these effects. While the simulations capture the overall trends, further refinement of material parameters is required for precise data fitting, which is beyond the scope of this study.

The carrier concentration profiles in the phototransistor (Figure 3b,c) reveal that illumination creates carrier concentration gradients in ADT, with hole accumulation and electron depletion at the heterojunction interface due to hole confinement in ADT and electron transfer to IGZO, respectively. A negative V_g further attracts holes in ADT and depletes electrons in IGZO near the SiO_2 interface. In IGZO, photogating primarily controls carrier concentration near the ADT interface, while V_g regulates it near the SiO_2 interface. Together, photogating and negative V_g create an electron concentration gradient across IGZO, with the total carrier concentration resulting from their combined effects.

At low-power photoexcitation ($1 \mu\text{W cm}^{-2}$, as considered in simulations), fewer photogenerated holes accumulate in ADT, resulting in weaker attraction of electrons in IGZO. Consequently, the applied V_g has a stronger influence on regulating IGZO conductance. Applying a negative V_g from 0 to -5 V efficiently depletes electrons throughout the IGZO layer, with a maximum reduction of over 15 orders of magnitude near the SiO_2 interface, as shown in Figure 3b. In contrast, high-power photoexcitation ($50 \mu\text{W cm}^{-2}$, as considered in simulations) generates a large number of holes confined in ADT, which strongly attract electrons in IGZO to the heterojunction interface, and maintain a high electron concentration there. As shown in Figure 3c, a more negative V_g is required to achieve the same electron depletion in IGZO as under low-power illumination. Even at $V_g = -5$ V, the electron concentration near the SiO_2 interface decreases by only ≈ 5 orders of magnitude, while the electron concentration near the ADT interface remains largely unaffected due to the strong electrostatic interaction with accumulated holes in ADT.

Under strong illumination, the photogating effect outweighs V_g in regulating the electron concentration in IGZO. Figure 3d shows the average electron concentration in IGZO as a function of V_g , highlighting that higher illumination power requires a more negative V_g to achieve the same level of electron depletion. Additionally, stronger illumination reduces the modulation efficiency of V_g , evident from the decreased slope of the curves. At a strong negative V_g , each curve saturates at a minimum electron concentration proportional to the illumination power density, suggesting that this concentration results from electron trans-

fer from ADT. The strong negative V_g also accumulates holes in IGZO, making their concentration comparable to electrons, with both carriers contributing to the off current. These findings effectively explain the progressive negative shift in threshold voltage and the corresponding increase in subthreshold swing observed with increasing photoexcitation power densities in Figure 2g,h.

It is worth noting that the dip in the electron concentration profiles in ADT arises from the optical power minimum, caused by interference-induced variations in optical power across the multilayer structure of the device. This variation is accurately modeled in the TCAD simulation using the transfer matrix method to account for the device structure's optical properties. The depth-dependent optical power creates non-uniform photogeneration rates in ADT, leading to varying photogenerated carrier concentrations throughout the depth of ADT. This effect is most noticeable at low carrier concentrations, particularly for minority electrons in ADT, and becomes less significant at higher photoexcitation power. Figure S6 (Supporting Information) shows the alignment between the minority electron concentration in ADT and the optical power intensity profile within the device.

The photogating effect and the applied V_g jointly regulate the electron concentration in IGZO. Proper selection of V_g is crucial to balancing these effects, ensuring efficient IGZO conductance modulation in response to illumination intensities for sensitive photodetection. As shown in Figure 3e, a fixed $V_g = 0$ V maintains a low hole concentration in ADT and a relatively high electron concentration in IGZO ($\approx 10^{13} \text{ cm}^{-3}$) without illumination. This reflects the Fermi level being near the mid-band gap of ADT and close to the conduction band edge in IGZO, as depicted in the energy band diagram under zero illumination in Figure 3f. Photoexcitation generates excess carriers in ADT, which subsequently induce carriers in IGZO through photogating and electron transfer. The added electrons in IGZO also elevate the minority hole concentration to maintain charge neutrality and stabilize internal electric fields. This is evidenced by the formation of electron (F_N) and hole (F_p) quasi-Fermi levels in both ADT and IGZO. Additionally, the hole accumulation in ADT lowers its energy potential, causing a slight tilt in the IGZO band and shifting the electron quasi-Fermi level closer to the conduction band edge. However, with the Fermi level initially near the conduction band edge without illumination, IGZO already has a high electron concentration, leaving limited room for further increases as the illumination power density rises. As a result, increasing the power density from zero to $10 \mu\text{W cm}^{-2}$ raises the electron concentration in IGZO to $\approx 10^{17} \text{ cm}^{-3}$, an increase of less than 4 orders of magnitude. This effect is further exacerbated under a positive V_g , further reducing the sensitivity of electron concentration changes to photoexcitation.

At a constant $V_g = -1$ V, without illumination the holes are initially accumulated in ADT through electrostatic attraction and IGZO is partially depleted, with the electron concentration reduced to 10^3 cm^{-3} , as shown in Figure 3g. The negative V_g allows the Fermi level to initially sit close to the HOMO of ADT and move toward the mid-band gap of IGZO under zero illumination in Figure 3h. The initial partial depletion of IGZO leaves a broader dynamic range for additional electron concentration to increase in response to photoexcitation. For instance, when the

power density increases to $10 \mu\text{W cm}^{-2}$, the electron concentration in IGZO rises to $\approx 10^{16} \text{ cm}^{-3}$, an increase of ≈ 13 orders of magnitude. The energy band diagram shows a noticeable rise in the electron quasi-Fermi level in IGZO from the mid-band gap to near the conduction band edge in response to the stronger photoexcitation.

A negative V_g of -5 V accumulates holes in ADT and strongly depletes electrons in IGZO, with the field effect of V_g governing the carrier concentrations. Under this condition, photoexcitation cannot further accumulate holes in ADT, which are necessary to modulate electron concentration in IGZO through the photogating effect, as shown in Figure 3i. The carrier concentration in IGZO increases proportionally with illumination power density, indicating that it is primarily contributed by electron transfer from ADT. The band diagrams in Figure 3j reveal that the large negative V_g keeps ADT at low electron potential, positioning the Fermi level very close to the HOMO of ADT and near the mid-band gap of IGZO. The steep slope of the IGZO band reflects the strong electric field in IGZO. The electron quasi-Fermi level shows little change in response to increasing photoexcitation power density.

Overall, the analysis concludes that achieving sensitive photodetection requires selecting an appropriate V_g that partially depletes IGZO, enabling the photogating effect to effectively modulate the electron concentration in IGZO.

At higher positive gate biases ($V_g > 4 \text{ V}$), the on-current showed a slight decreasing trend with increasing optical power density (Figure 2g,h). This phenomenon may be attributed to enhanced electron trapping at the ADT/IGZO interface under the combined influence of stronger optical excitation and positive V_g , further suppressing the on-current. Previous studies have reported that metal hydroxyl groups on the IGZO surface act as acceptor-like traps, efficiently capturing electrons and becoming negatively charged,^[41,42] thereby increasing the threshold voltage. This electron trapping effect may become more pronounced at the interface under stronger optical excitation and greater positive V_g due to two factors. First, the increased accumulation of photogenerated holes in ADT at the interface attracts more IGZO electrons, leading to enhanced electron trapping. Second, a higher positive V_g induces a larger number of majority electrons in IGZO when the transistor is in the on-state, enhancing the likelihood of electron trapping at the interface. This mechanism differs from the effect observed at negative V_g , where electron depletion dominates. A similar degradation in on-current due to electron trapping has been reported in IGZO TFTs.^[43] However, given the distinct materials and device structure in our study, further investigation is required to fully validate this mechanism, which will be explored in future research.

2.3. Phototransistor Performance and Transient Characteristics

The photosensor performance was evaluated using detectivity (D^*) and external quantum efficiency (EQE). Detectivity, expressed in $\text{cmHz}^{1/2}\text{W}^{-1}$ or Jones is calculated as:

$$D^* = \frac{R}{\sqrt{2qI_{\text{dark}}/A}} \quad (2)$$

where R (responsivity) is derived from Equation (1), I_{dark} is the dark current, A is the active area of the device, and q is the elementary charge. EQE is calculated as:

$$\text{EQE} = \frac{I_{\text{ph}} - I_{\text{dark}}}{q P_{\text{in}}/h\nu} = R \frac{h\nu}{q} \quad (3)$$

where $h\nu$ is the photon energy, and P_{in} is the incident optical power. The calculation of D^* assumes that the shot noise from the dark current is the dominant noise source limiting detectivity.^[44] The gate voltage-dependent detectivity of TEG-ADT/IGZO and TES-ADT/IGZO devices shown in Figure 4a,b demonstrates that maximum detectivity occurred at $V_g = -1 \text{ V}$ under green and blue excitation. Figure 4c highlights that the TEG-ADT/IGZO phototransistor achieved high detectivity from 450 to 650 nm, with a maximum value of 7.83×10^{13} Jones at 515 nm, while the TES-ADT/IGZO device reached a peak of 6.34×10^{13} Jones at 545 nm. The high detectivity is attributed to strong responsivity to green light and exceptionally low dark currents of 4 pA (Figure 2a). In contrast, the pristine IGZO device attained only 1.10×10^9 Jones between 450 and 650 nm. Both TEG-ADT/IGZO and TES-ADT/IGZO devices exhibited maximum EQEs of 675% and 518%, respectively, derived from their responsivities of 2.80 and 2.27 A W^{-1} (Figure 2d,e). These high efficiencies result from photocurrent amplification via the photogating effect, where photogenerated hole accumulation in ADT boosted the sensing current, yielding EQEs far exceeding 100%. Such characteristics position the devices as excellent candidates for low-power photosensor applications.

Figure 4d illustrates the photo-switching behavior of the phototransistors under a low-frequency 1 Hz pulsed excitation at 545 nm. The pristine IGZO device displayed minimal photoresponse with persistent photocurrent likely associated with the sub-bandgap tail state absorption. In contrast, both heterojunction phototransistors demonstrated significantly stronger photoresponse. Under pulsed optical excitation, the photocurrent rose rapidly with the light on and returned to the off state immediately after the light was turned off. The absence of persistent photocurrent, a common issue in oxide semiconductor photodetectors,^[39,45,46] was likely due to the top ADT layer blocking IGZO light absorption, ensuring that the photogating effect remained the primary source of photocurrent. Figure 4e shows the relationship between photocurrent density and illumination power density for the two heterojunction devices, highlighting a wide LDR across input light intensities. The LDR is calculated using the Equation (4):^[32]

$$\text{LDR} = 20 \log \frac{I_{\text{ph,max}}}{I_{\text{dark}}} \quad (4)$$

where $I_{\text{ph,max}}$ is the maximum photocurrent in the linear regime and I_{dark} is the dark current. Both phototransistors, illuminated at 545 nm, exhibited linear responses to optical power density over a range from 5×10^{-8} to $3.5 \times 10^{-4} \text{ W cm}^{-2}$. The TEG-ADT/IGZO device reached a $I_{\text{ph,max}}$ of 360 nA (0.36 mA cm^{-2}), while the TES-ADT/IGZO device achieved 460 nA (0.46 mA cm^{-2}). Both devices had an active area of 10^{-3} cm^2 and maintained a dark current of 4 pA. The calculated LDRs for TEG-ADT and TES-ADT heterojunction devices were 99.1 and 101.2 dB, respectively, outperforming

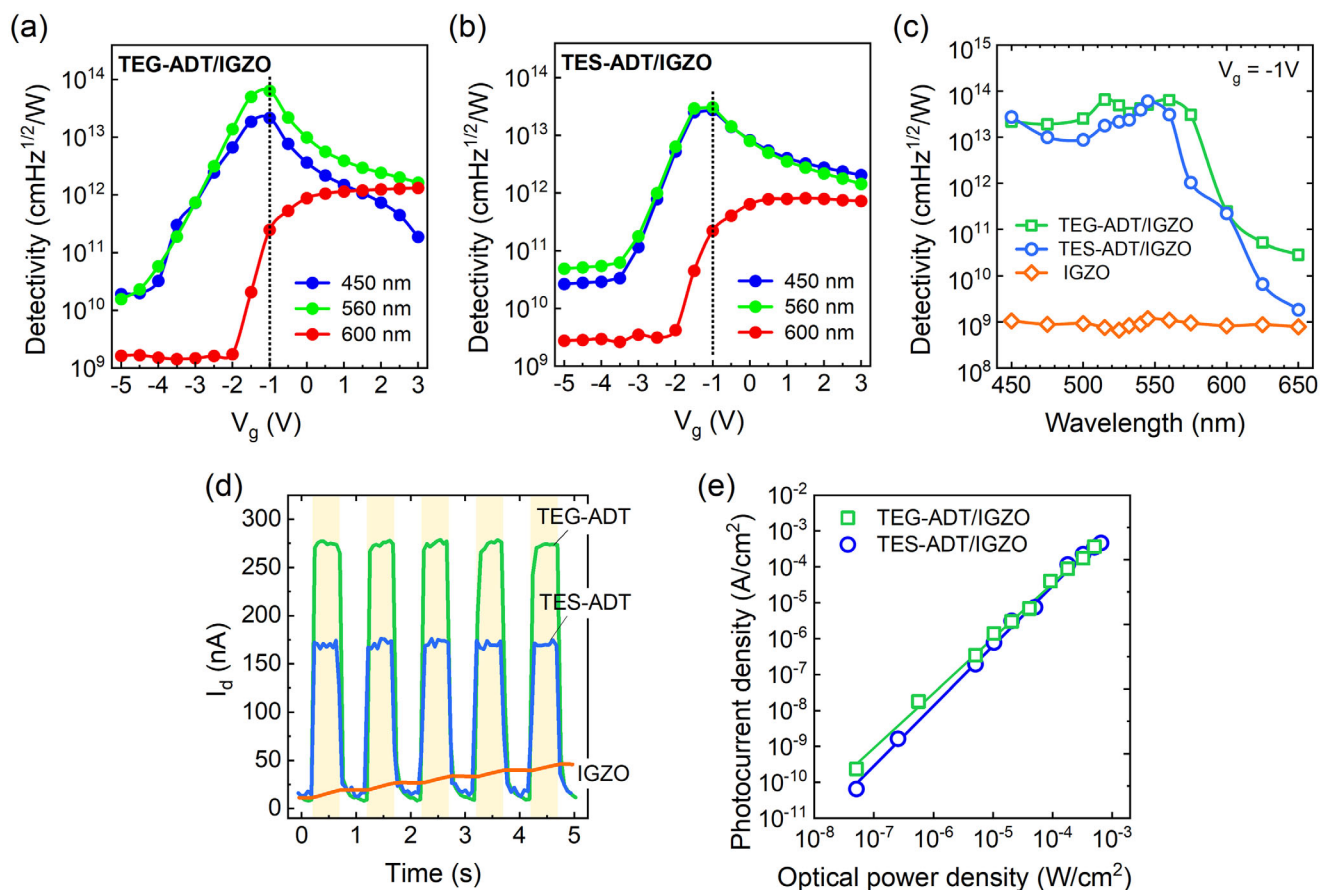


Figure 4. Detectivity of the a) TEG-ADT/IGZO and b) TES-ADT/IGZO phototransistors measured at various V_g and a fixed V_d of 5 V under 450, 560, and 600 nm illumination at $40 \mu\text{W cm}^{-2}$. c) Wavelength-dependent detectivity measured at $V_g = -1$ V for TEG-ADT/IGZO, TES-ADT/IGZO, and pristine IGZO phototransistors. d) Photo-switching response under 532 nm pulsed illumination at $350 \mu\text{W cm}^{-2}$ and $V_g = -1$ V. e) Photocurrent density of the heterojunction devices as a function of illumination power density, demonstrating an LDR exceeding 100 dB.

traditional InGaAs photodetectors (66 dB), and approaching the performance of Si photodetectors (120 dB).^[47] This enhanced performance can be attributed to their high sensitivity, enhanced photoresponse driven by the photogating effect, and exceptionally low dark current.

The transient light response of the phototransistors was evaluated under pulsed 525 nm LED illumination at 1 mW cm^{-2} with frequencies of 27 and 106 Hz (Figure 5). Both devices demonstrated fast photo-switching up to 100 Hz, with rise and fall times measured during a 27 Hz on-off cycle. The TEG-ADT/IGZO device (Figure 5a) exhibited rise and fall times of 3.5 and 9.5 ms, respectively, while the TES-ADT/IGZO device (Figure 5b) showed comparable times of 3.9 and 12.4 ms. Overall, these devices demonstrate faster response than most previously reported organic/IGZO-based heterojunction phototransistors, where response times typically exceed hundreds of milliseconds due to slow charge trapping and de-trapping processes at the interfaces.^[35] In our device, photogating was driven by a trap-free photogating mechanism involving the accumulation of photo-generated holes in the trap-reduced ADT in polymer blends, with assistance from a moderately negative V_g . Upon removal of

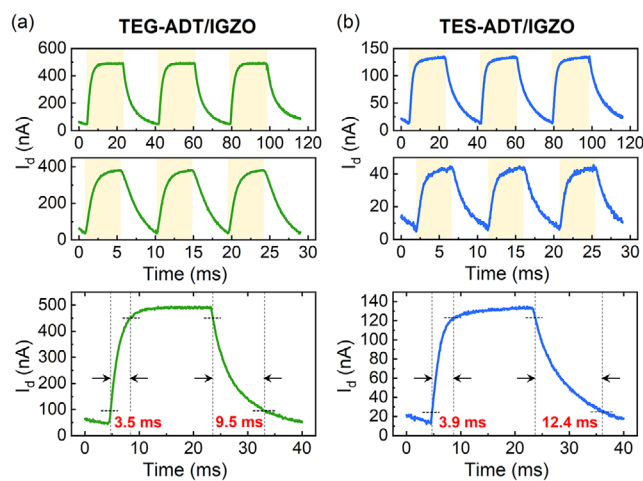


Figure 5. Transient photocurrent response of a) TEG-ADT/IGZO and b) TES-ADT/IGZO phototransistors under 525 nm pulsed illumination at 27 and 106 Hz, with a power density of 1 mW cm^{-2} . At 27 Hz, the rise and fall times are 3.5 and 9.5 ms for TEG-ADT/IGZO, and 3.9 and 12.4 ms for TES-ADT/IGZO.

photoexcitation, the accumulated hole recombined rapidly and the transfer curve promptly returned to its initial state (Figure S7, Supporting Information) without displaying a negative threshold voltage shift, which is typically associated with positive charge trapping at the interface. A comparison of the response time of our device with previously reported organic/IGZO-based heterojunction phototransistors (Table S3, Supporting Information) highlights the superior performance of our device relative to other organic/IGZO-based devices.^[32,48–50]

3. Conclusion

We demonstrated a high-performance organic-inorganic hybrid phototransistor using a type II heterojunction between photoactive ADT and photo-insensitive IGZO. This configuration facilitated electron transfer and enabled a photogating effect driven by the accumulation of photogenerated holes in ADT. Applying an appropriately tuned negative V_g was critical to gate the IGZO TFT into a partially depleted state within the subthreshold regime, enabling maximal detectivity and enhanced sensing current. Theoretical calculations were conducted to elucidate the device operation mechanism, providing insights that aligned well with the trend of experimental results. The devices achieved enhanced responsivity of 2.80 A W^{-1} and detectivity over 10^{13} Jones and an EQE of up to 675%. Additionally, the device exhibited a wide LDR exceeding 100 dB, a significantly suppressed dark current of 4 pA, and a rapid response time of less than 10 ms. These characteristics are on par with or surpass those of previously reported IGZO-based phototransistors. The suppressed dark current significantly reduces noise, enhancing the signal-to-noise ratio and detectivity, while the fast response time can support optical signal processing. With these high-performance metrics, the device is well-suited for advanced applications in machine vision and low-power photosensor technologies. These results underscore the potential of organic-inorganic hybrid systems to drive the development of next-generation photodetectors with outstanding performance.

4. Experimental Section

Material Preparation: Two types of di-fluorinated ADT derivatives, functionalized with either a side group of (triethylsilyl)ethynyl (TES) or (triethylgermyl)ethynyl (TEG), were separately mixed with poly(methyl methacrylate) (PMMA, m.w. = 15000, Polysciences Inc.) host polymer to create spin-coated films with an average molecular spacing of 1 nm.^[37] A 7.21 mg mL^{-1} toluene solution of PMMA was blended with either 11.60 mg mL^{-1} of TES-ADT or 13.31 mg mL^{-1} of TEG-ADT to produce the final mixed film.

Device Fabrication: The IGZO TFTs were fabricated on a 300 nm SiO_2 layer over a heavily doped p-type Si wafer, which served as the bottom gate. The substrates were first cleaned through sonication in acetone, isopropanol, and deionized water for 15 min each to remove surface contaminants. The samples were then nitrogen-dried and baked on a hot plate at $115 \text{ }^\circ\text{C}$ for 15 min. A 25 nm thick IGZO active layer was then deposited using radio frequency (RF) magnetron sputtering with a 3-inch target composed of indium, gallium, and zinc in a 1:1:1 molar ratio, patterned through a shadow mask. The sputtering process used a gas mixture of Ar and O_2 in a 20:1 ratio with an RF power of 75 W. The IGZO thin film underwent thermal annealing at $400 \text{ }^\circ\text{C}$ for 1 h in a muffle furnace for activation. The optimized O_2 partial pressure during IGZO sputtering, combined with precise annealing conditions, was essential to achieve a

low dark current and enhanced detectivity. Finally, 50 nm thick aluminum source and drain contacts, with a gap of $100 \mu\text{m}$ and a width of $1000 \mu\text{m}$, which defined the channel length and width, were deposited using thermal evaporation through a shadow mask. Before heterojunction formation, the IGZO TFT was baked at $115 \text{ }^\circ\text{C}$ for 15 min to remove any adsorbed water molecules, which can lead to charge trapping and threshold voltage shifts in IGZO TFTs. A 50 nm thick photosensitive organic layer, either TES-ADT in PMMA or TEG-ADT in PMMA, was then spin-coated onto the IGZO TFTs at 1500 rpm, resulting in TES-ADT/IGZO or TEG-ADT/IGZO organic-inorganic hybrid heterojunction TFTs. The devices were then baked at $85 \text{ }^\circ\text{C}$ in the dark for 10 min to remove residual solvent. All processes were conducted in a nitrogen-filled glovebox. Excess organic coating over the electrode pads was carefully removed using an acetone-soaked Q-tip. Finally, optical and electrical characterization of the device was performed under ambient conditions.

Optical and Electrical Characterization: The optical absorption of the device was measured using illumination from a tungsten halogen lamp, focused onto the sample with a 10x objective to create a near-diffraction-limited spot ($<5 \mu\text{m}$). Reflected light was collected and analyzed using a SpectraPro HRS-300 spectrograph. PL measurements were performed using 450 nm excitation from 100–180 fs pulses at 10 kHz, generated by a second-harmonic generation system (SHG, APE HarmoniXX), pumped by femtosecond pulses at 10 kHz from an optical parametric amplifier (OPA, ORPHEUS-F, Light Conversion). The excitation beam was focused on the sample and the PL was collected similarly to the absorption measurements, with a 500 nm long-pass filter to block the excitation beam. The I - V characteristics were measured using a Keithley 2636B sourceme-ter through a customized probing adapter. Wavelength-selective optical excitation was performed by coupling light from a Horiba FluoroMax 4 fluorospectrometer with an integrated monochromator and ozone-free xenon arc lamp. A neutral density filter ensured consistent power density across wavelengths. Transient photocurrent responses were captured using a Tektronix TBS 2000B series oscilloscope.

Supporting Information

Supporting Information is available from the Wiley Online Library or from the author.

Acknowledgements

The authors thank Prof. J. Anthony for the ADT derivatives and Rick Presley and Chris Tasker for their assistance with the RF sputtering and thermal evaporation tools. This work was supported in part by the National Science Foundation (NSF) (CHE-1956431 to O.O.). Sample characterization was partially performed in the NSF-MRI-funded user facility (DMR-1920368). Part of this research was conducted at the Northwest Nanotechnology Infrastructure, a National Nanotechnology Coordinated Infrastructure site at Oregon State University which is supported in part by the (grant NNCI-2025489) and Oregon State University.

Conflict of Interest

The authors declare no conflict of interest.

Data Availability Statement

The data that support the findings of this study are available in the supplementary material of this article.

Keywords

anthradithiophene, organic semiconductor, oxide semiconductor, photogating, phototransistors

Received: January 9, 2025
Revised: March 14, 2025
Published online:

- [1] Y. Xu, Q. Lin, *Appl. Phys. Rev.* **2020**, *7*, 011315.
 [2] A. Morteza Najarian, M. Vafaie, B. Chen, F. P. García de Arquer, E. H. Sargent, *Nat. Rev. Phys.* **2024**, *6*, 219.
 [3] K. Yao, M. Salvador, C.-C. Chueh, X.-K. Xin, Y.-X. Xu, D. W. deQuilettes, T. Hu, Y. Chen, D. S. Ginger, A. K.-Y. Jen, *Adv. Energy Mater.* **2014**, *4*, 1400206.
 [4] Y. Liu, C. Li, Z. Ren, S. Yan, M. R. Bryce, *Nat. Rev. Mater.* **2018**, *3*, 1.
 [5] K. Goushi, K. Yoshida, K. Sato, C. Adachi, *Nat. Photon* **2012**, *6*, 253.
 [6] C. Wang, H. Dong, W. Hu, Y. Liu, D. Zhu, *Chem. Rev.* **2012**, *112*, 2208.
 [7] Y. Tao, K. Yuan, T. Chen, P. Xu, H. Li, R. Chen, C. Zheng, L. Zhang, W. Huang, *Adv. Mater.* **2014**, *26*, 7931.
 [8] O. Ostroverkhova, *Chem. Rev.* **2016**, *116*, 13279.
 [9] K. J. Thorley, H. Le, Y. Song, J. E. Anthony, *J. Mater. Chem. C* **2022**, *10*, 15861.
 [10] W. Fudickar, T. Linker, *J. Am. Chem. Soc.* **2012**, *134*, 15071.
 [11] H. F. Haneef, A. M. Zeidell, O. D. Jurchescu, *J. Mater. Chem. C* **2020**, *8*, 759.
 [12] M. Ito, M. Kon, C. Miyazaki, N. Ikeda, M. Ishizaki, R. Matsubara, Y. Ugajin, N. Sekine, *Phys. Status Solidi* **2008**, *205*, 1885.
 [13] O. D. Jurchescu, S. Subramanian, R. J. Kline, S. D. Hudson, J. E. Anthony, T. N. Jackson, D. J. Gundlach, *Chem. Mater.* **2008**, *20*, 6733.
 [14] Z. A. Lampion, K. J. Barth, H. Lee, E. Gann, S. Engmann, H. Chen, M. Guthold, I. McCulloch, J. E. Anthony, L. J. Richter, *Nat. Commun.* **2018**, *9*, 5130.
 [15] Y. Mei, M. A. Loth, M. Payne, W. Zhang, J. Smith, C. S. Day, S. R. Parkin, M. Heeney, I. McCulloch, T. D. Anthopoulos, *Adv. Mater.* **2013**, *25*, 4352.
 [16] M. R. Niazi, R. Li, M. Abdelsamie, K. Zhao, D. H. Anjum, M. M. Payne, J. Anthony, D. Smilgies, A. Amassian, *Adv. Funct. Mater.* **2016**, *26*, 2371.
 [17] N. Shin, J. Kang, L. J. Richter, V. M. Prabhu, R. J. Kline, D. A. Fischer, D. M. DeLongchamp, M. F. Toney, S. K. Satija, D. J. Gundlach, B. Purushothaman, J. E. Anthony, D. Y. Yoon, *Adv. Funct. Mater.* **2013**, *23*, 366.
 [18] J. D. B. Van Schenck, G. Mayonado, J. E. Anthony, M. W. Graham, O. Ostroverkhova, *J. Chem. Phys.* **2020**, *153*, 164715.
 [19] A. D. Platt, J. Day, S. Subramanian, J. E. Anthony, O. Ostroverkhova, *J. Phys. Chem. C* **2009**, *113*, 14006.
 [20] K. Paudel, G. Giesbers, J. Van Schenck, J. E. Anthony, O. Ostroverkhova, *Org. Electron.* **2019**, *67*, 311.
 [21] W. Guo, Y. Liu, W. Huang, M. M. Payne, J. Anthony, H. E. Katz, *Org. Electron.* **2014**, *15*, 3061.
 [22] Z. Jagoo, Z. A. Lampion, O. D. Jurchescu, L. E. McNeil, *ACS Appl. Electron. Mater.* **2022**, *4*, 5799.
 [23] W. H. Lee, J. A. Lim, D. Kwak, J. H. Cho, H. S. Lee, H. H. Choi, K. Cho, *Adv. Mater.* **2009**, *21*, 4243.
 [24] M.-B. Madec, D. Crouch, G. Rincon Llorente, T. J. Whittle, M. Geoghegan, S. G. Yeates, *J. Mater. Chem.* **2008**, *18*, 3230.
 [25] M. R. Niazi, R. Li, E. Qiang Li, A. R. Kirmani, M. Abdelsamie, Q. Wang, W. Pan, M. M. Payne, J. E. Anthony, D.-M. Smilgies, S. T. Thoroddsen, E. P. Giannelis, A. Amassian, *Nat. Commun.* **2015**, *6*, 8598.
 [26] Z. Chen, S. Chen, T. Jiang, S. Chen, R. Jia, Y. Xiao, J. Pan, J. Jie, X. Zhang, *Nanoscale* **2024**, *16*, 3721.
 [27] W. E. B. Shepherd, A. D. Platt, D. Hofer, O. Ostroverkhova, M. Loth, J. E. Anthony, *Appl. Phys. Lett.* **2010**, *97*, 163303.
 [28] J. D. B. Van Schenck, E. K. Tanyi, L.-J. Cheng, J. Anthony, O. Ostroverkhova, *MRS Commun.* **2019**, *9*, 956.
 [29] S. Quan, L. Li, S. Guo, X. Zhao, D. Weller, X. Wang, S. Fu, R. Liu, Y. Hao, *ACS Appl. Mater. Interfaces* **2023**, *15*, 59592.
 [30] M. Liu, J. Wei, L. Qi, J. An, X. Liu, Y. Li, Z. Shi, D. Li, K. S. Novoselov, C.-W. Qiu, S. Li, *Nat. Commun.* **2024**, *15*, 141.
 [31] W. Chen, D.-C. Qi, H. Huang, X. Gao, A. T. S. Wee, *Adv. Funct. Mater.* **2011**, *21*, 410.
 [32] X. Xu, L. Yan, T. Zou, R. Qiu, C. Liu, Q. Dai, J. Chen, S. Zhang, H. Zhou, *ACS Appl. Mater. Interfaces* **2018**, *10*, 44144.
 [33] Y. S. Rim, Y. (Micheal) Yang, S.-H. Bae, H. Chen, C. Li, M. S. Goorsky, Y. Yang, *Adv. Mater.* **2015**, *27*, 6885.
 [34] T. Chen, S. Zhan, B. Li, B. Hou, H. Zhou, *Adv. Opt. Mater.* **2024**, *12*, 2302451.
 [35] D. Li, Y. Chen, Y. Tang, K. Liang, H. Ren, F. Li, Y. Wang, G. Liu, C. Song, L. Meng, B. Zhu, *ACS Appl. Electron. Mater.* **2023**, *5*, 578.
 [36] A. Ciavatti, L. Basiricò, I. Fratelli, S. Lai, P. Cosseddu, A. Bonfiglio, J. E. Anthony, B. Fraboni, *Adv. Funct. Mater.* **2019**, *29*, 1806119.
 [37] W. E. Shepherd, A. D. Platt, D. Hofer, O. Ostroverkhova, M. Loth, J. E. Anthony, *Appl. Phys. Lett.* **2010**, *97*, 163303.
 [38] P. Zhang, S. Samanta, X. Fong, *IEEE Trans. Electron Devices* **2020**, *67*, 2352.
 [39] H. Yoo, I. S. Lee, S. Jung, S. M. Rho, B. H. Kang, H. J. Kim, *Adv. Mater.* **2021**, *33*, 2006091.
 [40] J. Day, A. D. Platt, S. Subramanian, J. E. Anthony, O. Ostroverkhova, *J. Appl. Phys.* **2009**, *95*, 105.
 [41] C. Zhang, D. Li, P. T. Lai, X. D. Huang, *IEEE Electron Device Lett.* **2022**, *43*, 32.
 [42] X. D. Huang, Y. Ma, J. Q. Song, P. T. Lai, W. M. Tang, *IEEE Trans. Electron Devices* **2018**, *65*, 1009.
 [43] M.-Y. Tsai, T.-C. Chang, A.-K. Chu, T.-Y. Hsieh, T.-C. Chen, K.-Y. Lin, W.-W. Tsai, W.-J. Chiang, J.-Y. Yan, *Appl. Phys. Lett.* **2013**, *103*, 012101.
 [44] X. Gong, M. Tong, Y. Xia, W. Cai, J. S. Moon, Y. Cao, G. Yu, C.-L. Shieh, B. Nilsson, A. J. Heeger, *Science* **2009**, *325*, 1665.
 [45] S. Jeon, S.-E. Ahn, I. Song, C. J. Kim, U.-I. Chung, E. Lee, I. Yoo, A. Nathan, S. Lee, K. Ghaffarzadeh, J. Robertson, K. Kim, *Nat. Mater.* **2012**, *11*, 301.
 [46] S.-L. Gao, L.-P. Qiu, J. Zhang, W.-P. Han, S. Ramakrishna, Y.-Z. Long, *ACS Appl. Electron. Mater.* **2024**, *6*, 1542.
 [47] L. Dou, Y. (Micheal) Yang, J. You, Z. Hong, W.-H. Chang, G. Li, Y. Yang, *Nat. Commun.* **2014**, *5*, 5404.
 [48] H. Wang, Y. Xiao, Z. Chen, W. Xu, M. Long, J.-B. Xu, *Appl. Phys. Lett.* **2015**, *106*, 242102.
 [49] Z. Chen, G. Sheleg, H. Shekhar, N. Tessler, *ACS Appl. Mater. Interfaces* **2020**, *12*, 15430.
 [50] Y. J. Tak, D. J. Kim, W.-G. Kim, J. H. Lee, S. J. Kim, J. H. Kim, H. J. Kim, *ACS Appl. Mater. Interfaces* **2018**, *10*, 12854.